

# Rheological and Rheo-optical Behaviors of Nanocellulose Suspensions Containing Unfibrillated Fibers

Yoshifumi Yamagata (✉ [yoshifumi.yamagata@anton-paar.com](mailto:yoshifumi.yamagata@anton-paar.com))

Anton Paar Japan <https://orcid.org/0000-0002-2193-887X>

Shingo Niinobe

Shin-Etsu Chemical

Kotaro Suga

Anton Paar Japan

Keisuke Miyamoto

Anton Paar Japan

---

## Research Article

**Keywords:** nanocellulose, pseudo-plateau modulus, small angle light scattering (SALS), shear thinning, Guinier plot, power law

**Posted Date:** July 21st, 2021

**DOI:** <https://doi.org/10.21203/rs.3.rs-709626/v1>

**License:**  This work is licensed under a Creative Commons Attribution 4.0 International License.

[Read Full License](#)

---

**Version of Record:** A version of this preprint was published at Cellulose on March 15th, 2022. See the published version at <https://doi.org/10.1007/s10570-022-04509-6>.

**Rheological and Rheo-optical Behaviors of Nanocellulose Suspensions  
Containing Unfibrillated Fibers**

Yoshifumi Yamagata<sup>\*†</sup>, Shingo Niinobe<sup>\*\*</sup>, Kotaro Suga<sup>\*</sup> and Keisuke Miyamoto<sup>\*</sup>

*\* Anton Paar Japan K. K.,*

*Riverside Sumida 13F, 1-19-9, Tsutsumi-dori, Sumida-ku, Tokyo, Japan*

*\*\*Shin-Etsu Chemical Co., Ltd.,*

*28-1, Nishifukushima, Kubiki-ku, Joetsu-shi, Niigata, Japan*

†Corresponding Author: E-mail: [yoshifumi.yamagata@anton-paar.com](mailto:yoshifumi.yamagata@anton-paar.com)

+81-50-4560-2139

ORCID ID: 0000-0002-2193-887X

S. Niinobe e-mail: [niinobe@shinetsu.jp](mailto:niinobe@shinetsu.jp)

K. Suga e-mail: [kotaro.suga@anton-paar.com](mailto:kotaro.suga@anton-paar.com)

K. Miyamoto e-mail: [keisuke.miyamoto@anton-paar.com](mailto:keisuke.miyamoto@anton-paar.com)

## 23 **ABSTRACT**

24 Cellulose nanofibers (CNFs) produced by mechanical processing have a more uneven fiber shape, diameter, and length  
25 than those produced by chemical processing. Depending on the manufacturing conditions, CNFs containing insufficient  
26 fibrillated fibers may be produced. In order to find practical applications for CNFs containing unfibrillated fibers, it is  
27 important to understand how to control the rheological behavior of these systems. In this study, we investigated the  
28 relationship between the nanosized volume fraction and the rheological behaviors of CNF suspensions containing  
29 unfibrillated fibers prepared by a wet refining system (Water Jet System). The macroscopic structural changes in those  
30 suspensions under shear flow were also discussed based on rheo-optic measurements.

31 According to the frequency sweeps of the CNF suspensions, it was found that they were elastic-dominated gels, and the  
32 elasticity was attributed to the nanofibers. The elastic moduli increased with the volume fraction of the nanofibers,  
33 suggesting that the entanglement of the nanofibers was enhanced. The pseudo-plateau modulus  $G_p'$  is proportional to the  
34 nanofiber volume fraction, with the constant  $\alpha = 1.5$ , suggesting that the entropic elasticity is dominant.

35 The viscosity curves of the CNF suspensions showed a shear thinning behavior, in which the viscosity linearly  
36 decreased with the increasing shear rate. From the Rheo-SALS measured at the same time, we found that the aggregates  
37 of the nanofibers elongated in the flow direction and deformed into an elliptical shape with the applied shearing. The  
38 shape change of the aggregates comprised of the nanofibers became more pronounced with the increased nanofiber  
39 volume fraction. However, the effect of the shape change of the aggregates was hardly observed on the viscosity curve.

40 We speculate that this is due to the fact that the unnanosized fibers, which exhibit a Newtonian flow, play a significant  
41 role in the flow behavior of the CNF suspensions.

42

43

44 **KEYWORDS:** nanocellulose / pseudo-plateau modulus / small angle light scattering (SALS) / shear thinning / Guinier  
45 plot / power law

46

## 47 **Introduction**

48 Cellulose is the most prolific biological resource on earth, and it has been reported that terrestrial plants produce 100  
49 billion tons per year. Recently, cellulose has been reevaluated as an alternative biomass material to fossil materials  
50 because of its recyclability. In addition, the cellulose nanofiber (CNF) has attracted attention due to recent advances in  
51 nanotechnology. CNF is literally cellulose fibrillated to a nanoscale, and is expected to be used in a wide variety of fields,  
52 such as reinforcement materials for composites, heat insulators, optical and electronic devices, and medical materials, due  
53 to its light weight, high strength, and low linear thermal expansion coefficient (Eichhorn et al. 2010; Isogai et al. 2011;  
54 Klemm et al. 2011; Siqueira et al. 2010).

55 The manufacture of CNF can be roughly divided into chemical and mechanical treatments. As a chemical treatment,  
56 sulfuric acid has long been used in its manufacturing. In this method, cellulose fibers are treated at 30~40 °C for a long  
57 time to hydrolyze and remove the non-crystalline portions in order to obtain microcrystalline cellulose with the degree of  
58 polymerization of about 200~250. The product is called cellulose nanocrystal or cellulose nanowhisker. Recently, a  
59 catalytic oxidation method using TEMPO (2,2,6,6-tetramethylpiperidine-1-oxyl radical) has been proposed; the TEMPO  
60 catalytic oxidation was reported in the 1990s as a reaction that can regioselectively convert the C6 primary hydroxyl  
61 group of polysaccharides to carboxylate groups under mild conditions (Isogai and Kato 1998). The CNF obtained by the  
62 TEMPO oxidation had a uniform fiber width of a few nm and an ultra-fine, high-aspect-ratio shape with a length of  
63 several  $\mu\text{m}$ , and their suspensions were found to be transparent and highly viscous (Saito and Isogai 2004; Saito et al.

64 2007). The oxidation reaction introduces a high density of carboxyl and aldehyde groups to the cellulose fiber surface,  
65 however, which may modify the fiber surface (Saito et al. 2006) and change its properties, thus there is concern about the  
66 environmental impact associated with the chemicals.

67 On the other hand, mechanical treatment is a method to tear the cellulose fibers mainly in the axial direction by using  
68 shear and collision forces, and cavitation caused by rapid decompression. Mechanical devices, such as a high-pressure  
69 homogenizer (Iotti et al. 2011; Turbak et al. 1983; Yano and Nakahara 2004), aqueous counter-collision (ACC) method  
70 (Kose and Kondo 2011; Kose et al. 2011; Tsuboi et al. 2014), and Water Jet System (Watanabe et al. 2011) are used.

71 These mechanical methods caused high fibrillation by passing the fiber dispersion through the device many times, but in  
72 the case of the high-pressure homogenizers, pretreatment with enzymes is sometimes used because the fibers can clog the  
73 homogenizer and the energy consumption is high (Charani et al. 2013; Hayashi et al. 1998; Henriksson et al. 2007;  
74 Pääkkö et al. 2007). In the ACC method and the Water Jet System, cellulose dispersions are injected and collided with  
75 each other from opposite nozzles (injection speed: about 700 m/s, collision pressure: about 200 MPa), and the cellulose  
76 fibers are miniaturized only by the penetration force of the water between them. Although the force of collision is weaker  
77 than that of a covalent bond, the interaction between fibers is cleaved, thus the fibers can be nanosized without damaging  
78 the fiber surface. In addition, since all of these methods use only water and raw materials, the inherent properties of the  
79 raw materials, such as the degree of polymerization and crystallinity, can be maintained.

80 CNFs prepared from various types of cellulose sources using the above-mentioned process have been deployed in  
81 various industries due to their value-added properties, and studies have been conducted focusing on the rheological  
82 properties of the CNF suspensions (Bercea and Navard 2000; Boluk et al. 2011; Charani et al. 2013; Iotti et al. 2011;  
83 Iwamoto et al. 2014; Naderi et al. 2014; Pääkkö et al. 2007; Tanaka et al. 2020; Yamagata and Miyamoto 2021;  
84 Yamagata et al. 2020). In other words, it is important to understand how to control the rheological behavior of the CNF  
85 suspensions in order to fully exploit the potential of the material.

86 Factors that affect the rheological behavior of the CNF suspensions include the chemical composition of the fiber,  
87 including the surface functional groups, as well as the fiber shape and length distribution. Different starting materials  
88 have different chemical compositions, which results in a different fiber stiffness and interaction forces between the fibers.  
89 Therefore, even if the shape and the length distribution of the fibers are the same, the rheological behavior will be  
90 different depending on the fiber type. In addition, the viscosity and elastic modulus increase with the nanofiber  
91 concentration even if the starting material is the same (Charani et al. 2013; Iotti et al. 2011; Pääkkö et al. 2007; Yamagata  
92 et al. 2020).

93 However, there seems to be only a few quantitative and detailed studies of the effect of the fiber length distribution  
94 (containing poorly nanosized fibers) of the CNF on the rheological behavior. In particular, in the case of mechanical  
95 treatment, unlike chemical treatment, the shape, the diameter and the length of the produced CNF fibers are not uniform.  
96 From the viewpoint of reducing the production cost of CNF, it is important to find practical applications for the CNF that

97 contain fibers with insufficient nanosizing. In order to reduce the production cost of the CNF, it is essential to evaluate  
98 the physical properties of the CNF containing insufficiently nanosized cellulose fibers. In this study, we investigated the  
99 relationship between the CNF nanosized volume fraction and the rheological behavior of the CNF, which contain  
100 insufficiently nanosized fibers, and suspensions produced using a water-jet type wet refinement system. Furthermore,  
101 macroscopic structural changes of the CNF suspensions under shear flow were also discussed based on rheo-optic  
102 measurements.

103

## 104 **Experimental**

### 105 **Preparation of fibrillated cellulose**

106 Low-substituted hydroxypropyl cellulose (LODICEL®, Shin-Etsu Chemical Co., Ltd., hereinafter referred to as HPC)  
107 as the starting material, was added to ion-exchange water to prepare a dispersion of about 4 wt%. A water-jet type wet  
108 refinement device (Ultimaizer HJP25005, Sugino Machine Limited, Japan) was used as a mechanical refinement device,  
109 and the prepared dispersion was injected through two diamond nozzles (nozzle diameter: 0.13 mm) facing and collided  
110 with each other under a processing pressure of 180 MPa at room temperature (about 20 °C). The number of collisions  
111 was increased from 20 to 60 times to obtain the nanosized CNF suspensions.

### 112 **AFM observation**

113 CNF diluted with water to about a 0.001 wt% concentration was dropped onto a mica plate in a volume of about 1 mL,  
114 heated at 100 °C for 10 min, then air-dried at room temperature for a day and night. Fibers that adhered to the mica  
115 surface were obtained by this process. The samples were observed by an AFM system (Tosca 400, Anton Paar GmbH) in  
116 the tapping mode.

### 117 **Particle size distribution measurement**

118 The nanosized fibers were considered as spherical particles, and the particle size distribution was measured by a laser  
119 diffraction / scattering particle size analyzer (LS 13 320, Beckman Coulter, Inc.) equipped with a universal liquid sample  
120 module. The cumulative particle in the normal measurement range of 0.017~20,000  $\mu\text{m}$  were set as 100 %. Among them,  
121 the CNF particles volume fraction of 0.017~1.047  $\mu\text{m}$  automatically analyzed by the software was defined as the  
122 nanofiber volume fraction ( $V_n$ ).

### 123 **Rheometry**

124 Rheological measurements were carried out at 20°C by a stress-controlled rheometer, MCR-102 (Anton Paar GmbH).  
125 Parallel plates of 25 mm diameter with a 0.5 mm gap between them were used for the viscoelastic measurements. For the  
126 shear flow measurements, a quartz plate of 43 mm diameter with a 0.5 mm gap between them were used to measure the  
127 time dependence of the apparent viscosity  $\eta(\dot{\gamma})$  until a steady state was reached (1~5 min) at a fixed shear rate (Fig. S1).  
128 The effects of the sample evaporation were minimized by using a protective hood.

### 129 **Small Angle Laser Light Scattering (SALS)**

130 A small angle light scattering (SALS) system was attached to the above-mentioned rheometer and light scattering  
131 measurements were synchronously performed along with the viscosity measurements. A laser beam with a wavelength of  
132 658 nm was irradiated from the top of the rheometer onto a sample sandwiched between the quartz plates, and the  
133 transmitted scattered light was directly recorded on a CCD camera chip at the bottom of the instrument. All the exposure  
134 times were 8.5 ms.

135

## 136 Results and discussion

### 137 Length of CNF

138 Fig. 1 shows AFM images of the samples obtained after 20 and 60 collision times. The 20 collision times sample  
139 (Fig.1(a)) showed many fibers longer than several tens of microns, whereas the 60 collisions (Fig. 1(b)) showed few  
140 fibers longer than 10  $\mu\text{m}$ . In addition, fibers with a width of more than 1  $\mu\text{m}$  were observed in the 20 collision sample.  
141 However, it was difficult to accurately measure the fiber length from these images, so we measured the CNF fiber length  
142 by a laser diffraction / scattering size analyzer.

143

144

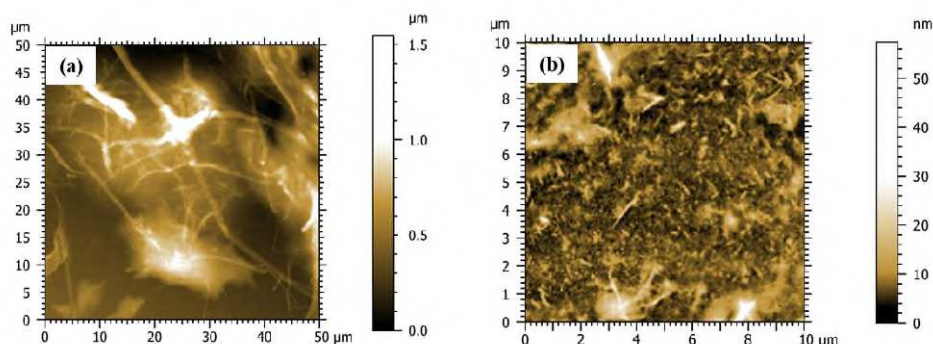
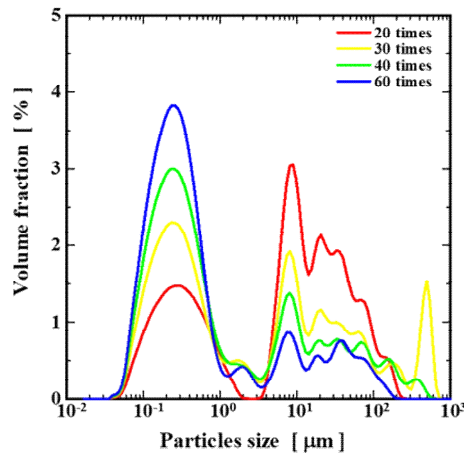


Fig.1 AFM images of CNF prepared with (a)20 and (b)60 collisions



**Fig. 2 Particle size distribution for CNF suspensions prepared by collision treatment**

145

146

147

148

149

150

151

152

153

154

155

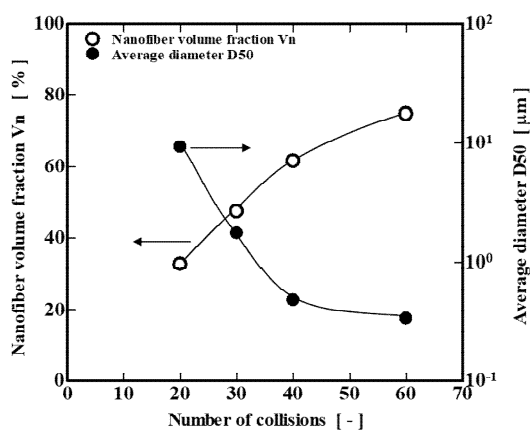
156

157

The laser diffraction / scattering method cannot accurately determine the fiber length of a fibrous sample, such as the CNF, because the particle size distribution is based on the light intensity distribution pattern of the diffracted / scattered light, which is calculated assuming that the particles are spherical. However, it is possible to obtain information based on the behavior (spread and size) in water reflecting the fiber length as a particle size distribution. Fig. 2 shows the particle size distributions of the CNF suspensions with the different number of collisions. All the samples showed a bimodal distribution, with a single peak centered at about 0.3  $\mu\text{m}$  and several peaks coexisting between 5 and 200  $\mu\text{m}$ . The peak (volume fraction) near about 0.3  $\mu\text{m}$  increased with the collision times, while the group of peaks coexisting at 5 to 200  $\mu\text{m}$  decreased. These results suggest that the peak of about 0.3  $\mu\text{m}$  and the multiple of peaks from 5 ~ 200  $\mu\text{m}$  correspond to the size of the nanofibers produced by mechanical treatment and the starting material, HPC, respectively.

The relationship between the nanofiber volume fraction ( $V_n$ ) smaller than about 1 mm and the number of collisions is shown in Fig. 3.  $V_n$  was 32.7 % for the 20 collisions, however,  $V_n$  increased with the number of collisions, reaching

158 74.8 % for the 60 collisions. At the same time, the cumulative medium diameter (D50) of the particles decreased by more  
 159 than one order of magnitude, from about 10  $\mu\text{m}$  at 20 collisions to about 0.3  $\mu\text{m}$  at 60 collisions. These results indicated  
 160 that a higher number of collisions is more effective for the nanosizing of the fibers.



161

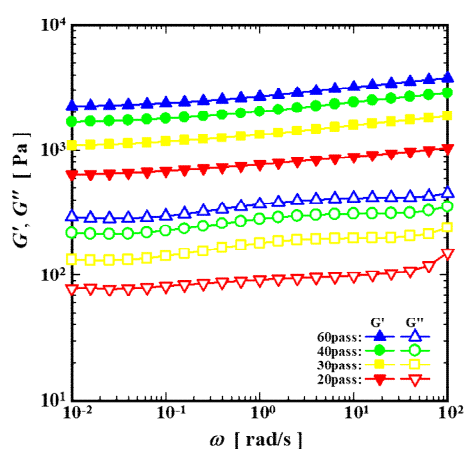
162 **Fig. 3 Nanofiber volume fraction Vn and average diameter, D50, of the CNF suspensions**

163 **versus the number of collisions**

164 **Viscoelastic behaviors of CNF suspensions**

165 Before measuring the frequency dependence of the viscoelasticity of the CNF suspensions, we performed the strain  
 166 sweeps to confirm the linear region. The results are shown in Fig. S2. Both the storage modulus  $G'$  and the loss modulus  
 167  $G''$  increased with the number of collisions, i.e., with the nanofiber volume fraction Vn. The critical strain for the  
 168 transition from linear to nonlinear was about 3 %, which was almost independent of Vn. Based on these results, the  
 169 frequency sweeps were measured with the strain fixed at 1 %. The results are shown in Fig. 4. All the CNF suspensions  
 170 have  $G' \gg G''$  over the entire measurement frequency range, and both  $G'$  and  $G''$  are almost independent of the frequency  
 171 ( $G' \approx \omega^0$ ,  $G'' \approx \omega^0$ ), thus it is considered that they are an elastic-dominated gel, and the elasticity is attributed to the

172 nanosized fibers. Thus, even for the sample with 20 collisions ( $V_n = 32.7\%$ ), it is suggested that the nanosized fibers  
 173 physically entangled to form a three-dimensional network structure. The storage modulus  $G'$  of the sample with 30  
 174 collisions ( $V_n = 47.4\%$ ) was about  $10^3$  Pa, which was similar to that of the 1.5 wt% suspension of CNF (fiber length:  
 175 827 nm, aspect ratio: 243) prepared by the TEMPO oxidation (Yamagata 2020) and the 2 % suspension of  
 176 microfibrillated cellulose (MFC) prepared by high-pressure homogenization by Iotti et al. (2011).

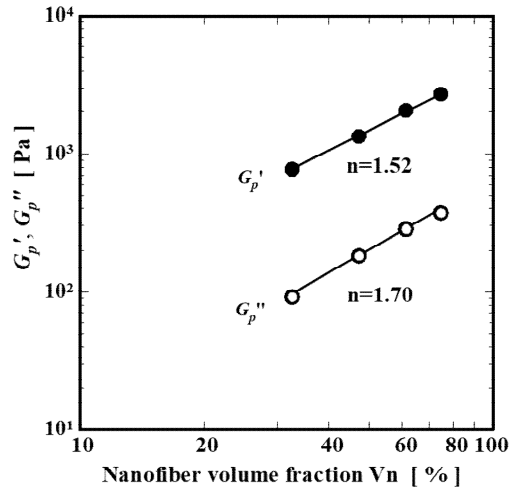


177  
 178 **Fig. 4 Frequency  $\omega$  dependence of storage modulus  $G'$  and loss modulus  $G''$  of CNF suspensions**

179 The relationship between the elastic moduli of CNF and the nanofiber volume fraction  $V_n$  was discussed. As already  
 180 mentioned, since  $G'$  and  $G''$  are almost independent of the frequency, the elastic moduli at  $\omega = 1$  rad/s are considered as  
 181 pseudo-elastic moduli ( $G_p'$ ,  $G_p''$ ). Both  $G_p'$  and  $G_p''$  increased with  $V_n$  as shown in Fig. 5. Many papers have reported  
 182 the dependence of the elastic modulus on the concentration in fiber suspension systems (Guenet 2000; Tamai et al. 2004;  
 183 Tatsumi et al. 2002). In most cases, a scaling law is observed between the modulus  $G$  and the concentration  $c$ , as shown  
 184 in Equation (1).

185 
$$G = Ac^\alpha \quad (1)$$

186 Here,  $A$  is a constant that depends on the modulus and the aspect ratio of the fiber itself, independent of the  
187 concentration  $c$ .  $\alpha$  is an index that reflects the network structure, and is reported to be about 2.25 in cellulose dispersion  
188 systems with a few  $\mu\text{m}$  fiber length regardless of the fiber type (Guenet 2000). The elastic moduli of the fibrillated CNF  
189 increased with  $V_n$  and depended on the nanofiber concentration. The values of  $\alpha$  for  $G_p'$  and  $G_p''$  were 1.5 and 1.7,  
190 respectively, which were lower than 2.25. Ramzi et al. found that the elastic modulus of the agarose cosolvent system can  
191 be represented by two straight lines with different exponents,  $\alpha = 1.5$  for the agarose concentration below 20 g/L and  $\alpha =$   
192 2.25 for the agarose concentration above 20 g/L (Ramzi et al. 1998). According to morphological observations, agarose  
193 gels are composed of nearly linear fibrillar arrays and are known to be intrinsically rigid materials (Sugiyama et al. 1940).  
194 In light of Jones and Marques's theory (Jones and Marques 1990), it is concluded that the agarose gel is rigid and has an  
195 enthalpic elasticity in low concentrations, but exhibits an entropic elasticity due to the binding sites between the fibers  
196 being disordered and flexible at high concentrations (Ramzi et al. 1998). Considering these facts, the gelation of  
197 suspensions of the mechanically fibrillated CNF is attributed to the increased entanglement of the nanosized fibers, and  
198 the entangled junctions are disordered and flexible, suggesting that the system as a whole is gel dominated by an entropic  
199 elasticity.



200  
 201 **Fig. 5 Pseudo-plateau moduli  $G_p'$  and  $G_p''$  at 1 rad/s of CNF suspensions as a function**  
 202 **of the nanofiber volume fraction  $V_n$**

203 **Shear flow behaviors of CNF suspensions**

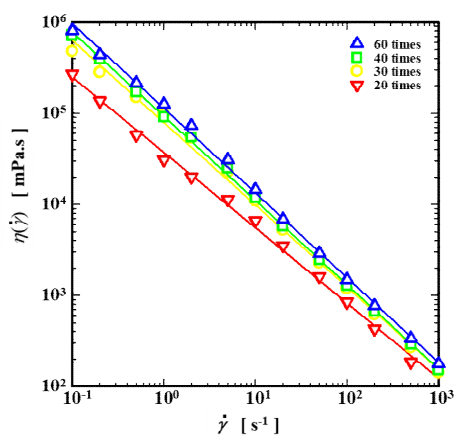
204 Fig. 6 shows the viscosity curves as a function of the shear rate for CNF suspensions prepared by 20 to 60 collisions.

205 The apparent viscosity  $\eta(\dot{\gamma})$  increased with the number of collisions in the entire measured shear rate range.  $\eta(\dot{\gamma})$  at  $\dot{\gamma} =$   
 206  $0.1s^{-1}$  was higher than 105 mPa.s for all samples, but  $\eta(\dot{\gamma})$  linearly decreased with the increasing  $\dot{\gamma}$ . At  $\dot{\gamma} = 1000 s^{-1}$ ,  $\eta(\dot{\gamma})$   
 207 decreased by three orders of magnitude to  $10^2$  mPa.s. These viscosity curves can be approximated by the power law  
 208 shown in Equation (2).

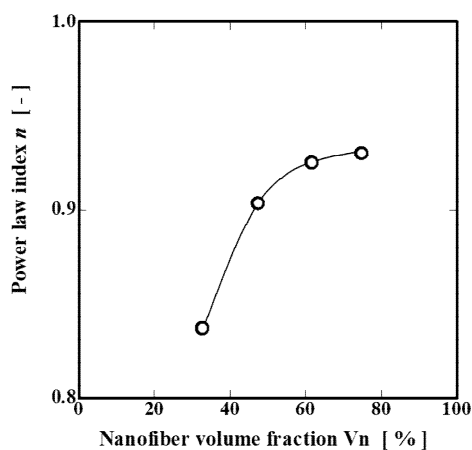
209 
$$\eta(\dot{\gamma}) = k\dot{\gamma}^{-n} \quad (2)$$

210 where, k and n are constants that have no physical meaning, but n is also called the power exponent coefficient, and  
 211 past papers have shown that  $n \leq 0.8$  for polymer solutions and melts, and  $n \approx 1$  for cohesive particle dispersion systems  
 212 and liquid crystals. The n-values of the CNF suspensions ranged from 0.84 to 0.93. When the n values were plotted

213 versus the nanofiber volume fraction  $V_n$ , the  $n$  values increased with  $V_n$  as shown in Fig. 7. This suggested that as the  
 214 number of nanofibers increased, the aggregation progresses with the entanglement of the fibers and the viscosity in the  
 215 near- stationary state also increased, but when the aggregated structure is destroyed by the applied shearing, the viscosity  
 216 decreases with the shear thinning behavior becoming more pronounced.



217  
 218 **Fig. 6 Viscosity curves for CNFs suspensions**



219  
 220 **Fig. 7 Power law index  $n$  versus nanofiber volume fraction  $V_n$**

221 Past studies about the rheological behavior of nanocellulose suspensions have confirmed that although they exhibit the  
 222 shear thinning behavior, where the apparent viscosity decreases with the increasing shear rate, the behavior is not

223 monotonically decreasing, but rather shows a complex behavior where the plateau of the apparent viscosity appears in the  
224 intermediate and high shear rate regions (Iotti et al. 2011; Li et al. 2015; Takai-Yamashita et al. 2021; Yamagata and  
225 Miyamoto 2021). According to the work of Li et al. (2015), the reason for the appearance of the apparent viscosity  
226 plateau in the intermediate and high shear rate regions is that the former is due to the formation of a more entangled  
227 network structure of oriented fibers by the applied shearing, and the latter is due to the disruption of most of the  
228 entangled network structure and the formation of a well-oriented structure. Iotti et al. (2011) also reported that the reason  
229 for the appearance of the viscosity plateau in the intermediate shear rate region is the shear-induced structure formation,  
230 i.e., since CNF is a long and thin fiber with a very high specific surface area covered by hydroxyl groups, the fibers are  
231 organized by being very close to each other in the structure, influencing the suppression of the decreasing viscosity. We  
232 also discussed the reason for the appearance of the viscosity plateau of the CNF suspensions prepared by the TEMPO  
233 oxidation based on the results of the Rheo-SALS measurements. CNF forms an almost isotropic circular (three-  
234 dimensionally spherical) aggregated structure in the low shear rate region. As the shear rate increases and reaches a  
235 critical value, the aggregation elongates in the flow direction and deforms into an anisotropic elliptical shape in order to  
236 reduce the flow resistance. We speculated that transient shear stress is generated at this time, suppressing the shear  
237 thinning behavior and appeared in the viscosity plateau region. In other words, the appearance of the viscosity plateau is  
238 considered to be caused by the organization and macroscopic structural changes of the nanosized CNF. However, the  
239 plateau region of the apparent viscosity was not observed on the viscosity curve of the mechanical nanosized CNF

240 suspensions. Therefore, we decided to perform Rheo-SALS measurements of the CNF suspensions containing  
241 insufficiently nanosized fibers to confirm whether there is any structural change in the CNF aggregations under shear  
242 flow.

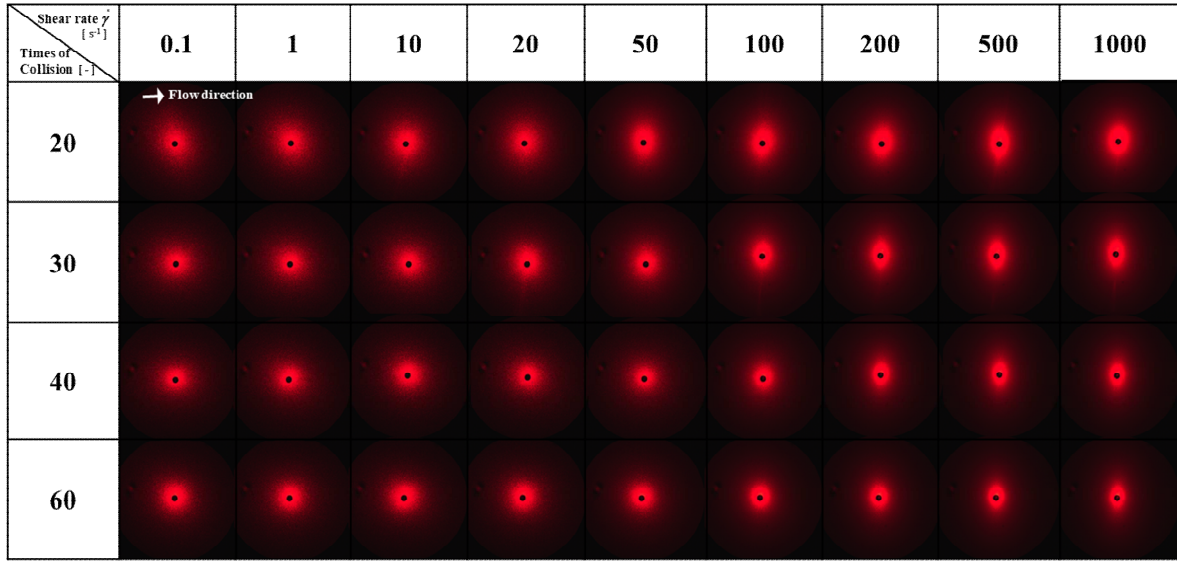
### 243 **Rheo-SALS measurements of CNF suspensions**

244 Small-angle light scattering (SALS) is one of the most widely used techniques to visualize changes in the internal  
245 structure of systems under shear flow by synchronizing it with rheological measurements. The intensity distribution of  
246 the scattered light caused by the incident primary laser beam is detected by a CCD camera during the light scattering.  
247 Various polarization components can be observed by changing the polarization directions of the incident light and the  
248 detector when making the measurements. The case where the polarization directions of the polarizer and the detector are  
249 orthogonal is called Hv, and the case where they are parallel to each other is called Vv. Based on the HV and VV  
250 scattering, we can obtain information about the optical anisotropy and density fluctuations and the optical anisotropy,  
251 respectively. The scattering images are omitted, but only the VV scattering results are shown below, since HV scattering,  
252 which indicates anisotropy, was rarely observed in the CNF suspensions.

253 Fig. 8 shows the scattering images obtained by the applied shearing from 0.1 to 1000 s<sup>-1</sup> to the CNF suspensions  
254 prepared by 20 to 60 collision times. The flow direction is from left to right in the scattering image. The scattering images  
255 showed an almost isotropic circular regardless of the number of collisions at a shear rate of 0.1 s<sup>-1</sup> as in the near static  
256 state. However, the scattering images transformed from a circular shape to a longitudinal elliptical shape extending

257 perpendicular to the flow direction with the increasing shear rate. At the high shear rate, the elliptical scattering images  
 258 became smaller with the number of collisions.

259 The shape and size of the scattered image are inversely related to those of the scatterers. In other words, a larger  
 260 scattering image means smaller scatterers, and an elliptical scattering image extending along the y-axis means an  
 261 elliptical scattering image extending along the x-axis (flow direction). We decided to calculate the size of the scatterer  
 262 from the scattering image, however, since it is too qualitative to discuss the change in the structure of the scatterers from  
 263 those of the scattering image.



264  
 265 **Fig. 8 Shear rate  $\dot{\gamma}$  dependence of scattering images of CNF suspensions**  
 266 **prepared with a different number of collisions**

267 **Internal structure change of CNF suspensions under shear flow by Rheo-SALS analysis**

268 The observed scattering images were imported into Anton Paar's software, NewSALS ver.2.01, and the scattering  
 269 intensity was calculated from the scattering vector  $q$ , which corresponds to the distance from the center of the transmitted

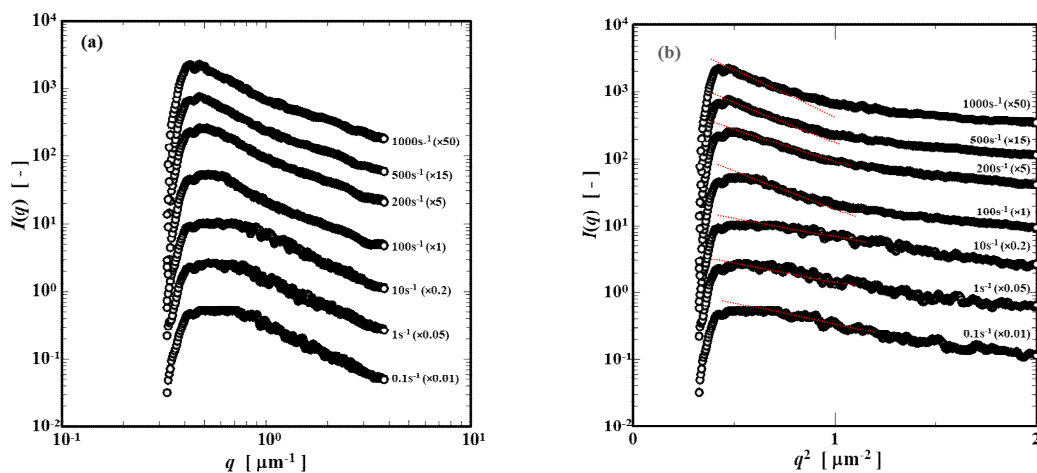
270 light, and the average value of the light intensity in a specific angular range ( $\pm 15^\circ$ ). The scattering intensity of CNF  $I(q)$   
 271 was calculated by subtracting those of water calculated in the same way. The scattering vector  $q$  can be calculated using  
 272 equation (3), and the effective range of  $q$  for this device is 0.171 to 4.131  $\mu\text{m}^{-1}$ .

$$273 \quad q = \frac{4\pi}{\lambda} \sin\left(\frac{\theta}{2}\right) \quad (3)$$

274 where  $\lambda$  is the wavelength of the laser beam (658 nm) and the scattering angle  $\theta$  was calculated by Equation (4).

$$275 \quad \theta = \tan^{-1}\left(\frac{\phi/2}{l}\right) \quad (4)$$

276  $l$  is the camera length (15 cm) and  $\phi$  is the size (length) of the scattering image.



277

278 **Fig. 9 (a) Scattering profiles and (b) Guinier plots for CNF suspension prepared**

279 **by 60 collisions (x-axis direction)**

280 **The curves are shifted vertically by the factor (0.01 ~ 50)**

281 Fig. 9(a) shows the scattering curves for the flow direction of  $0^\circ$  to the x-axis with 60 collisions, and parts of the

282 curves at the shear rate of 0.1 ~ 1000  $\text{s}^{-1}$  are extracted. In addition, the y-axis is shifted upward and downward by

283 multiplying the scattering intensity by an appropriate factor (0.01 ~ 50), since the scattering curves overlap and are  
284 difficult to understand. A plateau appeared around  $q = 0.4 \sim 0.7 \mu\text{m}^{-1}$  at the low shear rates of less than  $100 \text{ s}^{-1}$ . However,  
285 the plateau disappeared with the increasing shear rate, a maximum was observed around  $q = 0.4 \sim 0.5 \mu\text{m}^{-1}$  and the  
286 scattering intensity  $I(q)$  decreased toward the wide-angle side. The gradient of the decreasing  $I(q)$  becomes steeper with  
287 the increasing shear rate. The scattering function in the small-angle region where  $I(q)$  decreases can be approximated by  
288 Guinier's equation shown by Equation (5).

$$289 \quad I(q) = I_0 \exp\left(-\frac{R_g^2}{3} q^2\right) \quad (5)$$

290 Here  $I_0$  is the scattering intensity when extrapolated to  $q = 0$ , and  $R_g$  is the radius of gyration which is a measure of the  
291 size of the scatterers.  $R_g$  can be calculated from the slope of the straight line (red dashed line in Fig. 9(b)) when  $\ln I(q)$  is  
292 plotted versus  $q^2$  from Equation (6), and the slope increased with the shear rate. The Guinier approximation is said to be  
293 effective when the product of the scattering vector  $q_{\text{max}}$  at the right end of the linear approximation region of the  $\ln I(q)$  -  
294  $q^2$  curve and the calculated  $R_g$  is approximately 1.3 or less (Putnam et al. 2007; Zheng W and Best RB 2018). In our  
295 experimental systems,  $q_{\text{max}} \cdot R_g \approx 0.8 \sim 1.7$ , which is a rather high value, but the measured values slightly deviate upward  
296 from the approximate line, indicating that  $R_g$  may be underestimated. We believe that the variation of  $R_g$  with the shear  
297 rate and the number of collisions can be well discussed, however, because the characteristic known as the Guinier region  
298 in which the scattering intensity rapidly decreases from the plateau to the wide-angle region are observed on the  
299 scattering curves.

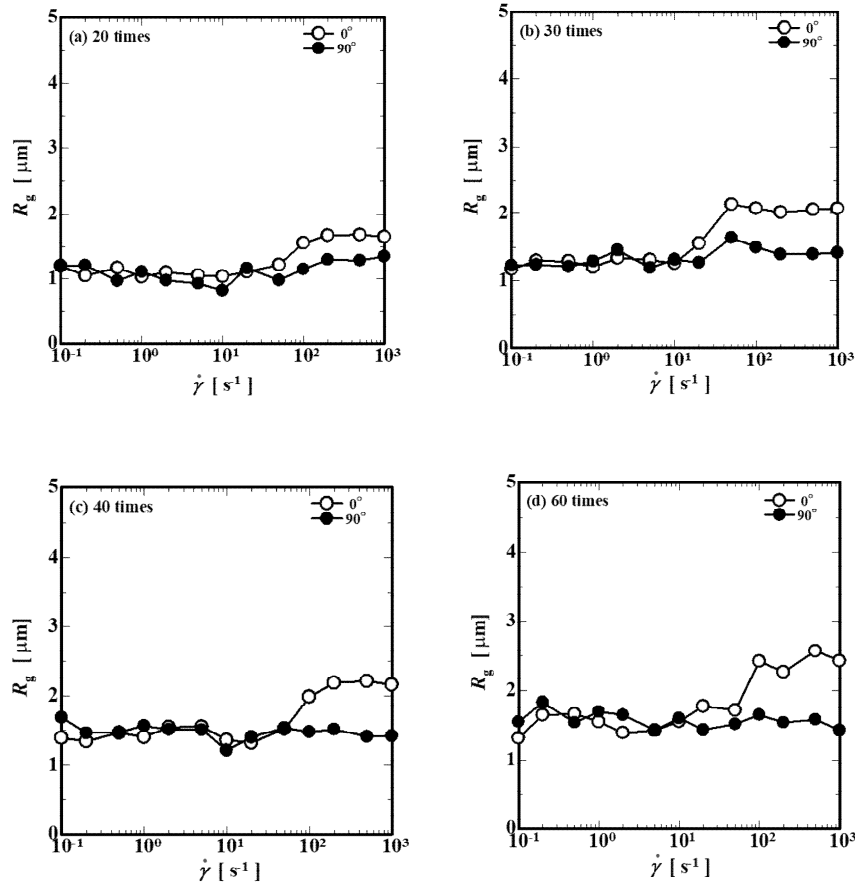
300 The shear rate dependence of the radius of gyration of the major and minor axes of the scatterers,  $R_g$ , obtained from  
301 Equation (5) is shown in Fig. 10. The ● and ○ plots in the Fig. 10 show the  $R_g$  of the scatterers obtained from the  
302 scattering intensity in the angle range of  $\pm 15^\circ$  with respect to the x- and y-axis, respectively. In other words, ●  
303 corresponds to the magnitude of the short axis of the scatterer oriented perpendicular to the flow direction, and ○  
304 corresponds to the magnitude of the long axis of the scatterers along the flow direction.

305  $R_g$  of the scatterers at the low shear rate was  $1.2 \mu\text{m}$  when the number of collisions was 20 (Fig. 9(a)). This size is  
306 smaller than that of the starting material HPC and larger than that of the fibrillated fibers. In other words, the size of the  
307 scatterer was inferred to be that of the cluster-like aggregates formed by entanglement of the nanofibers.  $R_g$  of the  
308 aggregates at low shear rates slightly increased with the number of collisions, but did not significantly change.

309 We now discuss the relationship between the size and shape of the aggregates and shear rate. In the case of 20  
310 collisions, the size of the aggregates in the flow direction ( $0^\circ$ ) and the vertical direction ( $90^\circ$ ) were almost equal and its  
311 shape seemed to be spherical below  $10 \text{ s}^{-1}$ . As the shear rate increased, however, the size in the flow direction increased  
312 to  $1.7 \mu\text{m}$  while the those in the vertical direction did not significantly change. Thus, the CNF aggregates elongated in the  
313 flow direction and deformed into an ellipse with the applied shearing. This shape change became more pronounced with  
314 the number of collisions, and the size of the aggregates in the flow direction grew to  $2.5 \mu\text{m}$  for the 60 collisions.

315 Fig. 11 shows the dependence of the average aspect ratio of the CNF aggregates at  $0.1 \sim 0.25$  and  $400 \sim 1000 \text{ s}^{-1}$  on  
316 the nanofiber volume fraction. As can be seen from the figure, the average aspect ratio of the aggregates showed a

317 constant value of about 1, which is a small concentration dependence, at the low shear rate, but increased with the  
 318 nanofiber volume fraction at the high shear rate. In other words, in the high shear rate region, the aggregates elongate  
 319 relatively more in the flow direction and the anisotropy increases with the increasing of nanofiber volume fraction.



320

321

322

**Fig. 10 Relationship between radius of gyration  $R_g$  and shear rate  $\dot{\gamma}$**

323

**Number of collisions; (a) 20, (b) 30, (c) 40, (d) 60**

324

Based on the above results, the mechanically fibrillated nanofibers formed an isotropic spherical agglomerated

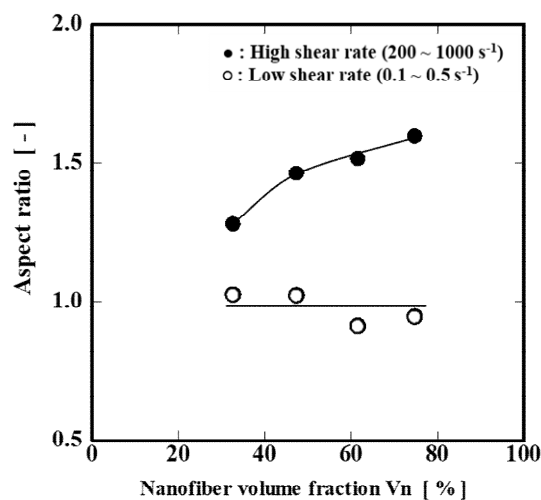
325

structure in the static state. In addition, its structure becomes slightly larger with the nanofiber concentration. The

326

aggregates deformed into an elliptical shape elongated in the flow direction with the applied shear rate above  $10 \text{ s}^{-1}$ , and

327 its deformation is more pronounced for the nanofiber concentration. Therefore, it is not surprising that the shear thinning  
 328 behavior is suppressed due to the transient shear stress induced by the shape change of the aggregates around  $10 \text{ s}^{-1}$ , and a  
 329 plateau region appears on the viscosity curves. However, no changes were observed on the viscosity curve. This is  
 330 probably due to the presence of long fibers with insufficient nanosizing. Fig. S3 shows the viscosity curve of a 4 wt%  
 331 dispersion of HPC, the starting material before the fibrillization. Fig. S3 shows the flow behavior of a 4 wt% dispersion  
 332 of HPC, the starting material before the fibrillization. The dispersion of the unfibrillated long fibers exhibits a Newtonian  
 333 flow, and the shear stress  $\sigma$  monotonically increases with the shear rate  $\dot{\gamma}$ . We speculated that the unnanosized long fibers,  
 334 which remained more than 25% even after 60 collisions, absorbed the transient stresses caused by the deformation of the  
 335 nanosized fiber aggregates, resulting in the monotonous shear thinning behavior of the CNF suspensions.



336

337 **Fig. 11 Relationship between aspect ratio of aggregates and nanofiber volume fraction  $V_n$**

338

339 **Conclusions**

340 The relationship between the nanofiber volume fraction and the rheological behaviors of CNF suspensions containing  
341 poorly nanosized cellulose fibers produced using a water-jet type wet refinement system was discussed. Based on the  
342 frequency sweep, we found that the CNF suspensions behaved like an elastic-dominated gel, and the nanosized fibers  
343 were responsible for development of the elasticity. The elastic moduli increased with the nanofiber volume fraction,  
344 suggesting that the entanglement of the fibers was enhanced. The pseudo-plateau modulus  $G_p'$  is proportional to the  
345 nanofiber volume fraction, and its constant  $\alpha = 1.5$ , indicating that the entropic elasticity is dominant.

346 The viscosity curve of the CNF suspensions showed a shear thinning behavior, in which the viscosity monotonically  
347 decreased with the shear rate. From the Rheo-SALS simultaneously measured, we found that the aggregates of the  
348 nanofibers elongated in the flow direction and deformed into an elliptical shape with the applied shearing. The shape  
349 change became more pronounced with the increasing nanofiber concentration, but the influence of those changes was  
350 hardly observed on the viscosity curves. We speculated that the unfibrillated fibers, which exhibit a Newtonian flow, are  
351 mostly responsible for the flow behavior of the CNF suspensions.

352 In conclusion, for the CNF suspensions containing poorly nanosized fibers, we speculated that the nanosized and  
353 unfibrillated fibers were largely responsible for the linear response under micro-deformation and the nonlinear response  
354 such as under shear flow, respectively.

355

356

357 **Authors contributions** Conceptualization: YY, SN, and KM; Data curation: YY and KM; Investigation: YY, SN, and  
358 KS; Project administration: YY; Resources: YY, SN, KS, and KM; Supervision: YY; Validation: YY, and SN;  
359 Visualization: YY, and KS; Writing—original draft: YY; Writing—review & editing: YY, SN, KS, and KM.

360

361 **Funding** There are not applicable.

362

363 **Data availability** All data generated or analyzed during this study are included in this published article and its  
364 supplementary information files.

365

366 **Compliance with ethical standards**

367 **Conflict of interest** The authors declare that there is no conflicts of interests/competing interests.

368 **Code availability** There is no code availability for software application or custom code.

369

## 370 REFERENCES

371 Bercea M, Navard P (2000) Shear dynamics of aqueous suspensions of cellulose whiskers, *Macromolecules*, 33:6011-  
372 6016. <https://doi.org/10.1021/ma000417p>

373 Boluk Y, Lahiji R, Zhaod L, McDermott MT (2011) Suspension viscosities and shape parameter of cellulose  
374 nanocrystals (CNC), *Colloids Surf A*. 377:297-303. <https://doi.org/10.1016/j.colsurfa.2011.01.003>

375 Charani PR, D-Firouzabadi M, Afra E, Shakeri A (2013) Rheological characterization of high concentrated MFC gel  
376 from kenaf unbleached pulp, *Cellulose*, 20:727–740. <https://doi.org/10.1007/s10570-013-9862-1> [19]

377 Eichhorn S J, Dufresne A, Aranguren M, Marcovich NE, Capadona JR, Rowan SJ, Weder C, Thielemans W, Roman M,  
378 Renneckar S, Gindl W, Veigel S, Keckes J, Yano H, Abe K, Nogi M, Nakagaito AN, Mangalam A, Simonsen J,  
379 Benight AS, Bismarck A, Berglund LA, Peijs T (2010) Review: current international research into cellulose  
380 nanofibers and nanocomposites, *J Mater Sci*, 45:1-33. <https://doi.org/10.1007/s10853-009-3874-0>

381 Guenet JM (2000) Structure versus rheological properties in fibrillar thermoreversible gels from polymers, *J Rheol*,  
382 44:947960. <https://doi.org/10.1122/1.551121> [27]

383 Hayashi N, Sugiyama J, Okano T, Ishiha M, (1998) The enzymatic susceptibility of cellulose microfibrils of the algal-  
384 bacterial type and the cotton-ramie type, *Carbohydr Res*, 305:261-269. [https://doi.org/10.1016/S0008-  
385 6215\(97\)10032-5](https://doi.org/10.1016/S0008-6215(97)10032-5) [16]

386 Henriksson M, Henriksson G, Berglund LA, Lindström T (2007) An environmentally friendly method for enzyme-  
387 assisted preparation of microfibrillated cellulose (MFC) nanofibers, *Eur Polym J*, 43:3434–3441.  
388 <https://doi.org/10.1016/j.eurpolymj.2007.05.038> [18]

389 Isogai A, Kato Y (1998) Preparation of polyuronic acid from cellulose by TEMPO-mediated oxidation, *Cellulose*, 5:153-  
390 164. <https://doi.org/10.1023/A:1009208603673>

391 Isogai A, Saito T, Fukuzumi H (2011) TEMPO-oxidized cellulose nanofibers, *Nanoscale*, 3:71-85.  
392 <https://doi.org/10.1039/c0nr00583e>

393 Iotti M, Gregersen ØW, Moe S, Lenes M (2011) Rheological studies of microfibrillar cellulose water dispersions, *J*  
394 *Polym Environ*, 19:137-145. <https://doi.org/10.1007/s10924-010-0248-2> [11]

395 Iwamoto S, Lee SH, Endo T (2014) Relationship between aspect ratio and suspension viscosity of wood cellulose  
396 nanofibers, *Polymer J*, 46:73–76. <https://doi.org/10.1038/pj.2013.64>

397 Jones JL, Marques CM (1990) Rigid polymer network models, *J Phys France*, 51:1113-1127.  
398 <https://doi.org/10.1051/jphys:0199000510110111300> [32]

399 Klemm D, Kramer F, Moritz S, Lindström T, Ankerfors M, Gray D, Dorris A (2011) Nanocelluloses: a new family of  
400 nature-based materials, *Angew Chem Int Ed*, 50:5438-5466. <https://doi.org/10.1002/anie.201001273>

401 Kose R, Kondo T (2011) Favorable 3S-network formation of chitin nanofibers dispersed in water prepared using aqueous  
402 counter collision, *Sen'i Gakkaishi*, 67:91-95. <https://doi.org/10.2115/fiber.67.91>

403 Kose R, Mitani I, Kasai W, Kondo T (2011) “Nanocellulose” as a single nanofiber prepared from pellicle secreted by  
404 *gluconacetobacter xylinus* using aqueous counter collision, *Biomacromolecules*, 12:716-720.  
405 <https://doi.org/10.1021/bm1013469>

406 Li M, Wu Q, Song K, Lee S, Qing Y, Wu Y (2015) Cellulose nanoparticles: Structure -morphology – rheology  
407 Relationships, ACS Sustainable Chem Eng, 3:821-832. <https://doi.org/10.1021/acssuschemeng.5b00144> [33]

408 Naderi A, Lindström T, Sundström J, (2014) Carboxymethylated nanofibrillated cellulose: rheological studies, Cellulose,  
409 21:1561-1571. <https://doi.org/10.1007/s10570-014-0192-8>

410 Pääkkö M, Ankerfors M, Kosonen H, Nykänen A, Ahola S, Österberg M, Ruokolainen J, Laine J, Larsson PT, Ikkala O,  
411 Lindström T (2007) Enzymatic hydrolysis combined with mechanical shearing and high-pressure homogenization  
412 for nanoscale cellulose fibrils and strong gels, Biomacromolecules, 8, 1934-1941.  
413 <https://doi.org/10.1021/bm061215p> [17]

414 Putnam CD, Hammel M, Hura GL, Tainer JA (2007) X-ray solution scattering (SAXS) combined with crystallography  
415 and computation: defining accurate macromolecular structures, conformations and assemblies in solution, Quarterly  
416 Reviews Biophysics, 40:191-285. <https://doi.org/10.1017/S0033583507004635>

417 Ramzi M, Rochas C, Guenet JM (1998) Structure-properties relation for agarose thermoreversible gels in binary  
418 solvents, Macromolecules, 31:6106-6111. <https://doi.org/10.1021/ma9801220> [30]

419 Saito T, Isogai A (2004) TEMPO-mediated oxidation of native Cellulose. The effect of oxidation conditions on chemical  
420 and crystal structures of the water-insoluble fractions, Biomacromolecules, 5:1983-1989.  
421 <https://doi.org/10.1021/bm0497769>

422 Saito T, Nishiyama Y, Putaux JL, Vignon M, Isogai A, (2006) Homogeneous suspensions of individualized microfibrils  
423 from TEMPO-catalyzed oxidation of native cellulose, *Biomacromolecules*, 7:1687-1691.  
424 <https://doi.org/10.1021/bm060154s>

425 Saito T, Kimura S, Nishiyama Y, Isogai A (2007) Cellulose nanofibers prepared by TEMPO-mediated oxidation of  
426 native cellulose, *Biomacromolecules*, 8:2485-2491. <https://doi.org/10.1021/bm0703970>

427 Siqueira G, Bras J, Dufresne A (2010) Cellulosic bionanocomposites: a review of preparation, properties and  
428 applications, *Polymers* 2:728-765. <https://doi.org/10.3390/polym2040728>

429 Sugiyama J, Rochas C, Turquois T, Taravel F, Chanzy H (1994) Direct imaging of polysaccharide aggregates in frozen  
430 aqueous dilute systems, *Carbohydrate Polym*, 23:261-271. [https://doi.org/10.1016/0144-8617\(94\)90188-0](https://doi.org/10.1016/0144-8617(94)90188-0) [31]

431 Takai-Yamashita C, Mabuchi Y, Senna M, Fuji M, Ohya Y, Yamagata Y (2021) Microstructure and surface activity of  
432 mechanically-dispersed cellulose nanofiber aqueous sol, *Cellulose*, 28:775-785. [https://doi.org/10.1007/s10570-](https://doi.org/10.1007/s10570-020-03570-3)  
433 [020-03570-3](https://doi.org/10.1007/s10570-020-03570-3) [34]

434 Tamai N, Tatsumi D, Matsumoto T (2004) Rheological properties and molecular structure of tunicate cellulose in LiCl /  
435 1,3-dimethyl-2-imidazolidinone, *Biomacromolecules*, 5:422-432. <https://doi.org/10.1021/bm034236h> [29]

436 Tanaka R, Kashiwagi Y, Okada Y, Inoue T (2020) Viscoelastic relaxation of cellulose nanocrystals in fluids:  
437 contributions of microscopic internal motions to flexibility, *Biomacromolecules*, 21:408–417.  
438 <https://doi.org/10.1021/acs.biomac.9b00943>

439 Tatsumi D, Ishioka S, Matsumoto T (2002) Effect of fiber concentration and axial ratio on the rheological properties of  
440 cellulose fiber suspensions, *Nihon Reoroji Gakkaishi (J Soc Rheol Jpn)*, 30:27-32.  
441 <https://doi.org/10.1678/rheology.30.27> [28]

442 Tsuboi K, Yokota S, Kondo T (2014) Difference between bamboo- and wood-derived cellulose nanofibers prepared by  
443 the aqueous counter collision method, *Nordic Pulp Paper Res J*, 29 69-76. [https://doi.org/10.3183/nppri-2014-29-](https://doi.org/10.3183/nppri-2014-29-01-p069-076)  
444 [01-p069-076](https://doi.org/10.3183/nppri-2014-29-01-p069-076)

445 Turbak AF, Snyder FW, Sandberg KR (1983) Microfibrillated Cellulose, a new cellulose product: properties, uses, and  
446 commercial potential, *J Appl Polym Sci : Appl Polym Symp*, 37:815-827.

447 Watanabe Y, Kitamura S, Kawasaki K, Kato T, Uegaki K, Ogura K, Ishikawa K (2011) Application of a water jet system  
448 to the pretreatment of cellulose, *Biopolymers*, 95:833-839. <https://doi.org/10.1002/bip.21686>

449 Yamagata Y, Miyamoto K, (2021) Rheo-optical analysis of aqueous suspension of cellulose nanofiber in shear flow  
450 field, *Nihon Reoroji Gakkaishi (J Soc Rheol Jpn)*, 49:199-206. <https://doi.org/10.1678/reology.49.199> [26]

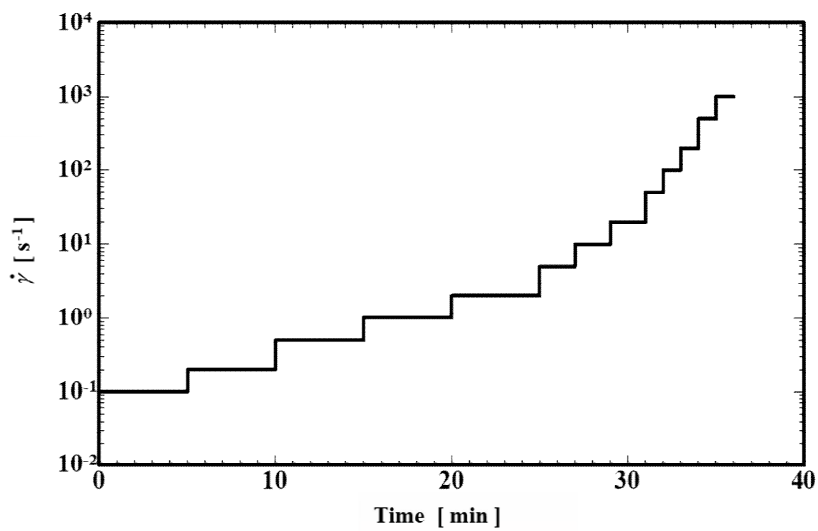
451 Yamagata Y, Suga K, Nakano Y, Takasaki Y, Miyamoto K (2020) Aspect ratio of temp-oxidized nanocellulose and  
452 rheological analysis of aqueous suspensions, *Nihon Reoroji Gakkaishi (J Soc Rheol Jpn)*, 48:207-213.  
453 <https://doi.org/10.1678/rheology.48.207>

454 Yano H, Nakahara S, (2004) Bio-composites produced from plant microfiber bundles with a nanometer unit web-like  
455 network, *J Mater Sci*, 39:1635-1638. <https://doi.org/10.1023/B:JMSC.0000016162.43897.0a>

456 Zheng W, Best RB (2018) An extended Guinier analysis for intrinsically disordered proteins, *J Mol Biol*, 430:2540-2553.

457 <https://doi.org/10.1016/j.jmb.2018.03.007>

459

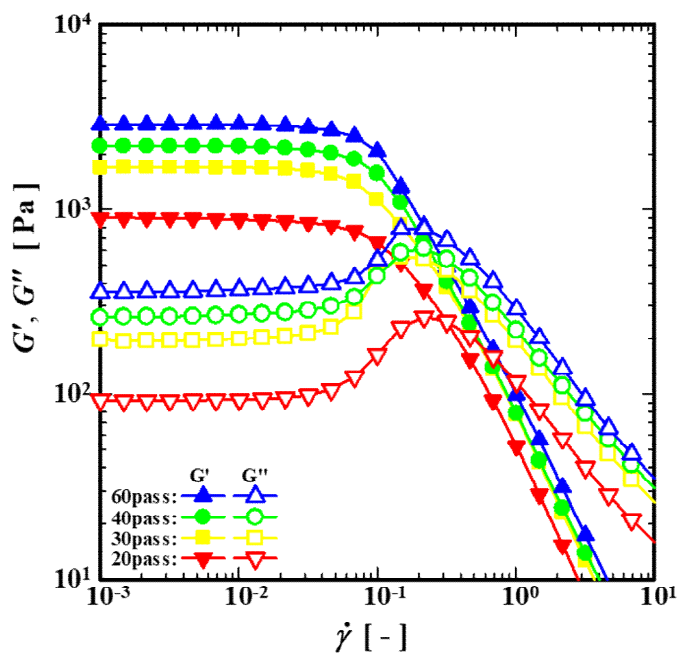


460

461

Fig. S1 Measurement program for steady flow.

462

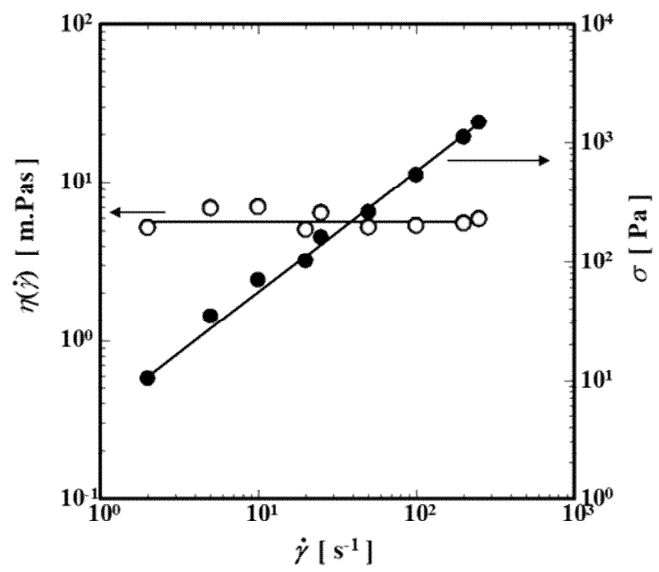


463

464

Fig. S2 Strain dependence of dynamic moduli  $G'$  and elastic  $G''$ .

465



466

467

Fig. S3 Viscosity curve of 4 wt% HPC suspension without mechanical treatment.

468

$\circ$ :  $\eta(\dot{\gamma})$       $\bullet$ :  $\sigma$

## Supplementary Files

This is a list of supplementary files associated with this preprint. Click to download.

- [SupplementaryMaterials.pptx](#)